This article has been accepted for publication in a future issue of this journal, but has not been fully edited. Content may change prior to final publication. Citation information: DOI 10.1109/TUFFC.2019.2945636, IEEE Transactions on Ultrasonics, Ferroelectrics, and Frequency Control

Source Density Apodisation: Image Artefact Suppression through Source Pitch Non-Uniformity

Erwin J. Alles and Adrien E. Desjardins

***Abstract*—Conventional ultrasound imaging probes typically comprise finite-sized arrays of periodically spaced transducer elements, which in the case of phased arrays can result in severe grating and side lobe artefacts. Whereas side lobes can be effectively suppressed through amplitude apodisation ("AmpA"), grating lobes arising from periodicity in transducer placement can only be suppressed by decreasing the element pitch, which is technologically challenging and costly. In this work, we present source density apodisation ("SDA") as an alternative apodisation scheme, where the spatial source density (and hence the element pitch) is varied across the imaging aperture. Using an all-optical ultrasound imaging setup capable of video-rate 2D imaging as well as dynamic and arbitrary reconfiguration of the source array geometry, we show both numerically and experimentally how SDA and AmpA are equivalent for large numbers of sources. For low numbers of sources, SDA is shown to yield superior image quality as both side and grating lobes are effectively suppressed. In addition, we demonstrate how asymmetric SDA schemes can be used to locally and dynamically improve the image quality. Finally, we demonstrate how a non-smoothly varying spatial source density (such as that obtained for randomised arrays or in the presence of source positioning uncertainty or inaccuracy) can yield severe image artefacts. The application of SDA can thus yield high image quality even for low channel counts, which can ultimately result in higher imaging frame rates using acquisition systems of reduced complexity.**

I. Introduction

Current ultrasound imaging probes typically comprise electronic transducer elements that utilise piezoelectric or capacitive transduction mechanisms [1]. Due to fabrication constraints, these transducer elements are commonly arranged rigidly in periodically spaced arrays [2]. For phased array imaging probes in which the transducer element pitch obeys the spatial Nyquist limit (i.e., the pitch is less than half the central acoustic wavelength) [2], such arrays can yield images of high quality and low artefact levels. For high frequency imaging probes, however, achieving the Nyquist-dictated maximum element pitch is technologically challenging and costly. As a result, many current high frequency imaging probes comprise transducer elements that are larger than half the central acoustic wavelength [2]. Combined with a periodic transducer element spacing, this results in the formation of grating lobes that can lead to image artefacts. In addition, imaging arrays have necessarily finite spatial extents. The resulting discontinuities at the edges of the imaging aperture result in the formation of side lobes [2], which can result in further image artefacts.

Side lobes are commonly suppressed through the application of amplitude weighting functions (dubbed here as amplitude apodisation: "AmpA") that reduce the contribution of the elements located towards the edges of the aperture to the image. This method of apodisation is effective [2], but typically results in a reduced lateral resolution due to an apparent reduction in the aperture dimensions. However, grating lobes are unaffected by amplitude apodisation and can only be suppressed by decreasing the element pitch or by avoiding spatial periodicity; both solutions are technologically challenging using conventional electronic transducers.

Recently, an all-optical alternative to electronic ultrasound transducers has been presented that uses light to both transmit and receive ultrasound. Using fibre optic technology, optical ultrasound sources [3–8] and detectors [9–14] are readily miniaturised, exhibit high bandwidths and sensitivities, and are immune to electromagnetic interference. Recently, a benchtop system has been demonstrated that used a single fibre optic ultrasound detector and a centimetre-scale monolithic photoacoustic ultrasound generator membrane to achieve video-rate two-dimensional imaging [15]. Through the use of lenses and a rapidly steerable mirror, arbitrary control over the location of the optical focus (and hence over the location of the ultrasound source) was achieved, which enabled the synthesis of ultrasound source arrays of arbitrary and reconfigurable configuration, including arrays comprising spatially overlapping sources. In previous work, this benchtop system was used to show how tapering the spatial source density towards the edges of the aperture (a technique dubbed source density apodisation: "SDA") significantly improved the image quality compared to conventional periodic source spacing [15, 16]. In this work, we present the theoretical framework behind both AmpA and SDA, and compare AmpA and SDA for a range of apodisation windows using both numerical and experimental phantom data. In addition, we explore whether asymmetric SDA schemes can improve the image quality locally and dynamically.

EJ Alles and AE Desjardins are with the Department of Medical Physics & Biomedical Engineering, University College London, Malet Place Engineering Building, London WC1E 6BT, United Kingdom, as well as with the Wellcome/EPSRC Centre for Interventional and Surgical Sciences, Charles Bell House, University College London, 43-45 Foley Street, London W1W 7TS, United Kingdom. Correspondence address: E.Alles@UCL.ac.uk. The authors wish to thank Dr Efthymios Maneas for providing the tissue mimicking phantom, and gratefully acknowledge the support of NVIDIA Corporation with the donation of the Quadro P6000 GPU used for this research. This work was supported by the Wellcome/EPSRC Centre for Interventional and Surgical Sciences (WEISS) (203145Z/16/Z), an Innovative Engineering for Health award by the Wellcome Trust (Grant No. WT101957), and the Engineering and Physical Sciences Research Council (EPSRC) (EP/N021177/1).

0885-3010 (c) 2019 IEEE. Personal use is permitted, but republication/redistribution requires IEEE permission. See http://www.ieee.org/publications_standards/publications/rights/index.html for more information.

This article has been accepted for publication in a future issue of this journal, but has not been fully edited. Content may change prior to final publication. Citation information: DOI 10.1109/TUFFC.2019.2945636, IEEE Transactions on Ultrasonics, Ferroelectrics, and Frequency Control

II. Methods

Optical ultrasound generation and detection

Ultrasound was generated optically *via* the photoacoustic effect [17]. Pulsed excitation light (wavelength: 1064 nm, pulse duration: < 5 ns, pulse energy: 76 µJ, pulse repetition rate: 3 kHz, beam diameter: 1.0 mm; FQS-400-1-Y-1064, Elforlight, U.K.) was delivered to an ultrasound generator membrane (comprising a nanocomposite of multi-walled carbon nanotubes and polydimethylsiloxane (PDMS) [5, 15]), where it was converted into ultrasound (pressure at the membrane surface: 0.98 ± 0.06 MPa; center frequency: 15.0 MHz; -6 dB bandwidth: 27.1 ± 2.2 MHz). Using a cylindrical lens (focal length: 50 mm; LJ1695RM-C, Thorlabs, Germany), the excitation light was confined to an eccentric focal spot, resulting in an eccentric optical ultrasound source (dimensions: 224 ± 53 µm laterally by 1.1 mm ± 82 µm elevationally) that generated an elevationally collimated ultrasound field to maximise the signal-to-noise ratio at depth. Using a steerable mirror, the optical focus (and correspondingly the ultrasound source) was scanned across the generator membrane to synthesise a one-dimensional source aperture of arbitrary geometry (aperture width: 13 mm; synthesis rate: 2000 ultrasound source locations per second). Each source location was excited sequentially to synthesise the imaging aperture, and the back-scattered ultrasound was detected and digitised for each source location (250 MSa/s, 14-bit, no signal averaging; M4i.4420-x8, Spectrum, Germany) using a single, stationary fibre-optic detector positioned centrally within the imaging plane at an axial offset of 0.4 mm. This detector comprised a plano-concave Fabry-Pérot cavity at its distal end (noise-equivalent pressure: 40 Pa, bandwidth: 80 MHz, near-omni-directional response for frequencies up to 20 MHz, [18]), of which the optical reflectivity was modulated by impinging ultrasound waves [14]. The back-scattered pressure was recorded by accurately monitoring the sensor's optical reflectivity, as described in detail by Alles *et al.* (2018) [15]. The experimental setup was controlled using a custom LabVIEW script (LabVIEW 2014, National Instruments, TX, USA) and is shown schematically in Fig. 1.

Numerical simulations

Numerical simulations of the pulse-echo wave propagation were performed using the spatial impulse response method. The source transducers were approximated by rectangles measuring 200 µm $\times$ 1 mm, and their impulse responses were computed using the FOCUS package [19, 20]. The temporal excitation of the acoustic source was modelled as a Hann-weighted tone burst (centre frequency: 15 MHz; duration: 4 cycles) that was matched to the power spectrum of the generated ultrasound. The pressure field generated by source i scatters off point scatterers located in $\vec{r}_j$, and the back-scattered pressure is recorded by a point detector (assuming omni-directionality and a flat frequency response) located in $\vec{r}_r$. For source i, the recorded pulse echo pressure

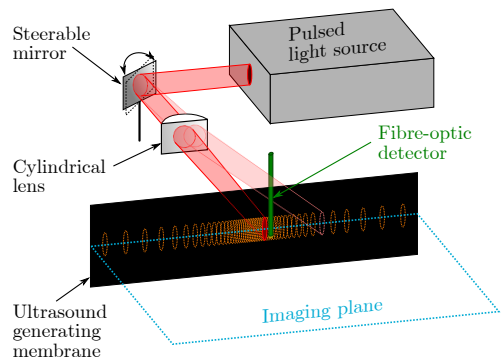

Fig. 1. **Schematic of the experimental setup (not to scale).** Excitation light is focussed onto an ultrasound generator membrane through a cylindrical lens, and a steerable mirror is used to translate the focal spot across the membrane and thus synthesise a one-dimensional ultrasound source aperture of arbitrary geometry. The two optical paths shown correspond to two separate ultrasound source locations that are sequentially excited. Back-scattered ultrasound waves are recorded using a single stationary fibre-optic detector.

trace is hence given by:

$$p_{r,i}(t) = \sum_{j=1}^{N_{\text{scat}}} \frac{R_j}{|\vec{r}_j - \vec{r}_r|} p_i \left(\vec{r}_j, t - \frac{|\vec{r}_j - \vec{r}_r|}{c} \right), \qquad (1)$$

where R_j is the reflectivity of the j-th point scatterer, the summation extends over all N_{scat} point scatterers, c is the homogeneous speed of sound, and $p_i(\vec{r}_j, t)$ is the pressure generated by source i as computed using the impulse response method. B-scans were simulated by computing separate pulse echo pressure traces $p_{r,i}(t)$ for all sources i. White noise was added to all simulated pulse-echo pressure traces computed in this work at a signal-to-noise ratio of 20 dB to match the SNR observed experimentally after envelope detection.

Image reconstruction

Images were reconstructed through dynamic focussing using the Delay-and-Sum (DAS) algorithm [21, 22], in which the image amplitude $I(\vec{r})$ in image position $\vec{r}$ is given by

$$I(\vec{r}) = \sum_{i=1}^{N_{\text{src}}} W_i \; p_{r,i} \left(t = \frac{|\vec{r} - \vec{r}_r| + |\vec{r} - \vec{r}_{s,i}|}{c} \right), \qquad (2)$$

where $p_{r,i}(t)$ is the pressure generated by the i-th source located in $\vec{r}_{s,i}$ as detected by a single detector located in $\vec{r}_r$, W_i is an optional AmpA window function, and N_{src} is the number of sources distributed across the source aperture. The speed of sound c was estimated from the continuously monitored temperature of the water bath (USB-TC01, National Instruments, TX, USA) [23]. Equation (2) represents the coherent summation of the pulse-echo pressures detected for all sources; as such, amplitude and phase effects (such as attenuation, source directionality and temporal signatures of the sources and detector) are omitted.

Equation (2) was implemented on a Quadro P6000 GPU (Nvidia Corporation, CA, USA) using the CUDA 10.0

0885-3010 (c) 2019 IEEE. Personal use is permitted, but republication/redistribution requires IEEE permission. See http://www.ieee.org/publications_standards/publications/rights/index.html for more information.

This article has been accepted for publication in a future issue of this journal, but has not been fully edited. Content may change prior to final publication. Citation information: DOI 10.1109/TUFFC.2019.2945636, IEEE Transactions on Ultrasonics, Ferroelectrics, and Frequency Control

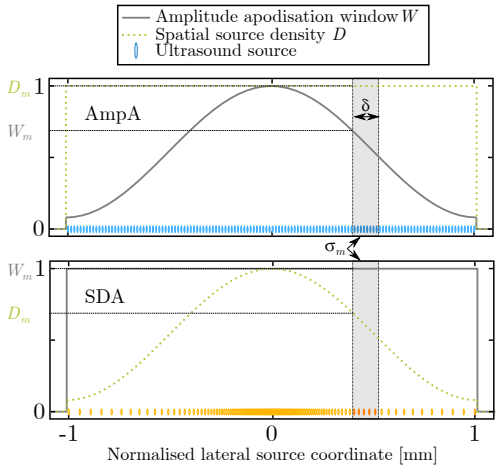

Fig. 2. **Visual representation of amplitude and source density apodisation.** In the case of amplitude apodisation (AmpA, top), the ultrasound sources are equidistantly spaced, resulting in a constant spatial source density D, and a spatially varying amplitude apodisation window W is applied. In the case of source density apodisation (SDA, bottom), the amplitude apodisation window is held constant across the aperture, whilst varying the spatial source density. In either case, the contribution of the set of sources σ_m to the image can be approximated by the product of the size of the source set (the number of sources contained within the strip) with the spatial source density D_m and the amplitude apodisation amplitude W_m at the start of the strip (cf. Eq. 4).

parallel computing platform. Parallelisation was achieved by distributing the computation of the image pixels to individual threads. The computation was performed in single precision using 128 blocks and 1024 threads per block; these parameters were determined empirically to yield the best performance. To ensure responsiveness of the custom LabVIEW user interface during image reconstruction, the image was divided in subsets of 2^{17} pixels that were sequentially reconstructed using multiple CUDA function calls. Compared to the same code run on a single CPU (Core i7-6700, 3.4 GHz, Intel, CA, USA), the GPU implementation reduced the time required to reconstruct an image by a factor of 89.6. To further improve the image frame rate, image reconstruction of the current frame and acquisition of the next B-scan were performed in parallel.

III. Apodisation schemes

For a one-dimensional source array (i.e., $\vec{r}_{s,i} = (x_{s,i}, 0, 0)$), the contribution of a narrow lateral strip m of width δ to the total image (see Fig. 2) is given by

$$I(\vec{r})_m = \sum_{i \in \sigma_m} W_i \; p_{r,i}(\tau_i), \tag{3}$$

where set $\sigma_m = \{k \mid x_{s,m} \leq x_{s,k} < x_{s,m} + \delta\}$, and the notation $\tau_i = (|\vec{r} - \vec{r}_r| + |\vec{r} - \vec{r}_{s,i}|)/c$ was introduced for brevity. When this strip is sufficiently narrow, pressure $p_{r,i}(\tau_i) \approx p_{r,m}(\tau_m)$ and AmpA apodisation window $W_i \approx W_m \equiv W(x_{s,m})$ are approximately constant across the strip, hence

$$I(\vec{r})_m \approx p_{r,m}(\tau_m) W_m \; \text{size}(\sigma_m) \approx p_{r,m}(\tau_m) W_m \; \delta D_m, \tag{4}$$

where $D_m \equiv D(x_{s,m})$ is the spatial source density (i.e., the number of sources per unit distance), which is computed in practice by counting the number of sources within each strip. The total image is now obtained by summing the contributions of all strips m,

$$I(\vec{r}) = \sum_{m=1}^{M} I(\vec{r})_m = \sum_{m=1}^{M} W_m \; \delta D_m \; p_{r,m}(\tau_m), \tag{5}$$

where $M = A/\delta$ is the total number of strips and A is the aperture size. For a periodically spaced source array, $D(x_{s,i}) = N_{\text{src}}/A$ is constant. If, in addition, $\delta = A/N_{\text{src}}$ is set to the source pitch, Eq. (5) reduces to the classical DAS expression of Eq. (2), as each strip contains exactly one source.

Equation (5) reveals how apodisation can be achieved through two separate mechanisms: either by applying a weighting function $W(x)$ (corresponding to conventional AmpA), or by applying a spatially varying spatial source density $D(x)$ (corresponding to SDA). The two mechanisms can be combined to obtain hybrid apodisation schemes. In the limiting case where $N_{\text{src}} \to \infty$, the AmpA and SDA schemes are equivalent: changing either the weighting function $W(x)$ or the spatial source density $D(x)$ by some amount results in the same difference in contribution of strip m to the total image.

For finite numbers of sources, however, the discretely sampled pressure $p_{r,i}(\tau_i)$ depends on the lateral source coordinate $x_{s,i}$, which in turn depends on the spatial source density $D(x)$. As a result, the total image $I(\vec{r})$ obtained using just AmpA will differ from that obtained using SDA alone, regardless of the apodisation functions, aperture size and number of sources. This difference is more pronounced for arrays comprising small numbers of sources, where the difference in the set of source coordinates $x_{s,i}$ between arrays employing either AmpA or SDA is larger.

Common choices for apodisation windows include top hat ($W = 1$, corresponding to no amplitude apodisation), Hamming, Hann, Gaussian, Blackman, cosine [2] and an exponentiated normalised hyperbolic sine function [24], each of which results in a different trade-off between lateral resolution and side lobe level. These windows can be applied to achieve both AmpA and SDA: for AmpA, the window W is applied as a weighting function during image reconstruction. For SDA, the window D is computed for N_{src} equidistantly distributed positions across a normalised aperture ranging between ± 1. The non-equidistantly spaced lateral source coordinates are then obtained through numerical integration of the reciprocal of the spatial source density, followed by normalisation and scaling to the physical aperture width.

In the case of AmpA, the imaging performance of these apodisation windows can for monochromatic waves be predicted from the power spectrum of the apodisation window function W [2]. Since AmpA and SDA were shown above to be mathematically equivalent, the imaging performance of an SDA apodisation function D can hence similarly be predicted from its power spectrum. However, due to the large ultrasound bandwidths generated in this work, the achieved imaging

0885-3010 (c) 2019 IEEE. Personal use is permitted, but republication/redistribution requires IEEE permission. See http://www.ieee.org/publications_standards/publications/rights/index.html for more information.

This article has been accepted for publication in a future issue of this journal, but has not been fully edited. Content may change prior to final publication. Citation information: DOI 10.1109/TUFFC.2019.2945636, IEEE Transactions on Ultrasonics, Ferroelectrics, and Frequency Control

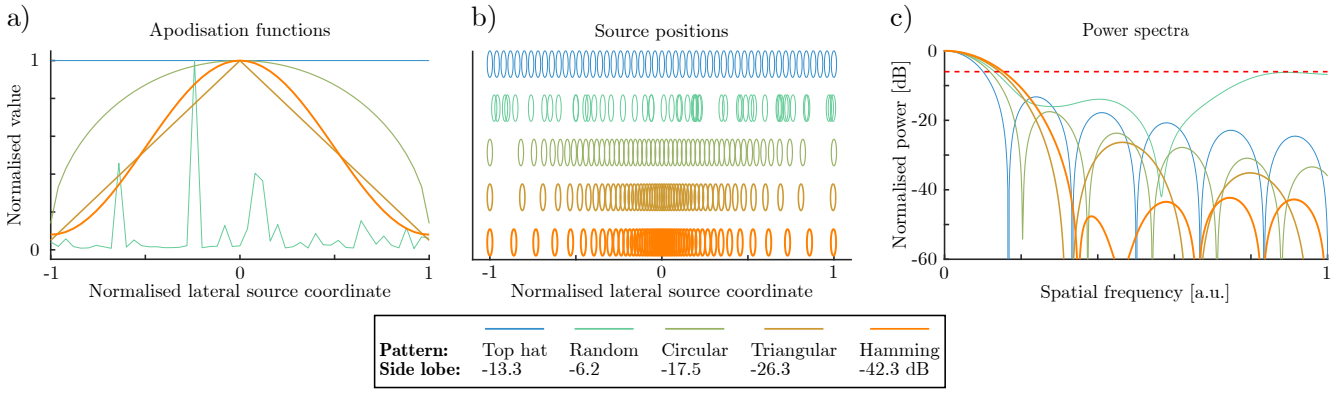

Fig. 3. **Sample apodisation schemes. a)** The apodisation functions for five apodisation schemes: top hat, random, circular, triangular, and Hamming. In the case of conventional amplitude apodisation (AmpA) these apodisation functions are applied as weighting factors during image reconstruction; in the case of source density apodisation (SDA) these functions are applied as spatial source densities from which the source locations are computed. **b)** Geometries of the ultrasound source arrays resulting from (top to bottom): top hat, random, circular, triangular and Hamming SDA. The source distribution for each SDA scheme contains just 51 sources to improve visibility. **c)** Normalised power spectra corresponding to the apodisation functions. The width of the main lobe (i.e., the first crossing with the -6 dB power level indicated in red) is predictive of the lateral resolution of the resulting image; the side lobe level is indicative of the magnitude of the side lobe artefacts in the resulting image. The maximum side lobe levels are listed in the legend.

performance will deviate from monochromatic predictions based on power spectra.

As an illustration, the apodisation windows and corresponding power spectra of five apodisation schemes are shown in Fig. 3. For this comparison, the following apodisation windows were used: top hat (resulting in a constant source pitch), random (where the lateral source coordinate $x_{s,i}$ is randomised across the aperture to avoid periodicity and the associated grating lobes), circular (where the apodisation window is given by the circle equation $D^2(x) + x^2 = 1$, yielding the previously considered array geometry where the lateral source coordinates are given by the trigonometric asin function [15]), triangular, and Hamming (a window commonly applied in AmpA). As can be observed, each apodisation scheme results in a different main lobe width (resulting in a different lateral resolution) and different side lobe level (resulting in a different image clutter level). As a trend, the side lobe level and main lobe width were observed to be inversely proportional, and lower side lobe levels are generally achieved at the expense of a reduced lateral resolution. The use of randomised source coordinates results in very high side lobe levels (in this instance -6.2 dB), and hence very poor image contrast is expected for this apodisation function.

IV. Results

Amplitude apodisation versus source density apodisation

Simulated all-optical ultrasound images of a single point scatterer reveal that, for top hat AmpA and top hat SDA, increasing the number of sources (and hence reducing the spatially invariant source pitch) improves the image quality as grating lobes are suppressed when the spatial Nyquist condition is met (Fig. 4). However, the side lobes are unaffected by the source pitch, and can only be suppressed by applying additional AmpA. In contrast, when SDA is applied, both grating lobes and side lobes are strongly suppressed, even for very low numbers of sources. The remaining image artefacts are due to the image reconstruction algorithm, as DAS works by virtue of coherent summation across the aperture. Noise and other artefacts are assumed to be zero-mean and incoherent, so that they sum to zero amplitude. This assumption is increasingly inaccurate for low numbers of sources; in practice, reconstruction artefacts will appear in addition to grating and side lobe artefacts. A finite bandwidth contributes to these artefacts, as does a low spatial source density, either locally or globally.

Performance of various source density apodisation schemes

Applying different SDA schemes whilst imaging the same cross-section of a phantom allowed for direct comparison of the performance of these apodisation schemes. Using an array of point scatterers as an imaging phantom (Fig. 5), the resolution and clutter level were compared for the five apodisation functions considered in Fig. 3 in both simulated and experimentally obtained images. As can be observed, top hat SDA achieved the best lateral resolution, and increasingly lower lateral resolutions were achieved using random, circular, triangular and Hamming SDA. In contrast, circular, Hamming and triangular SDA achieved similar image contrasts, whereas top hat and especially random SDA yielded significantly higher artefact levels. Good agreement was observed between simulation and experiment for the image resolution; however, experimentally obtained images consistently yielded lower image contrast. The additional artefacts in experimentally obtained images were due to slight inaccuracies and uncertainty in the source locations, which are investigated in greater detail in the following section. In simulations, point scatterers were modelled as mathematical points; in experiments, point scatterers were approximated by placing two parallel layers of tungsten wires (diameter: 27 µm;

0885-3010 (c) 2019 IEEE. Personal use is permitted, but republication/redistribution requires IEEE permission. See http://www.ieee.org/publications_standards/publications/rights/index.html for more information.

This article has been accepted for publication in a future issue of this journal, but has not been fully edited. Content may change prior to final publication. Citation information: DOI 10.1109/TUFFC.2019.2945636, IEEE Transactions on Ultrasonics, Ferroelectrics, and Frequency Control

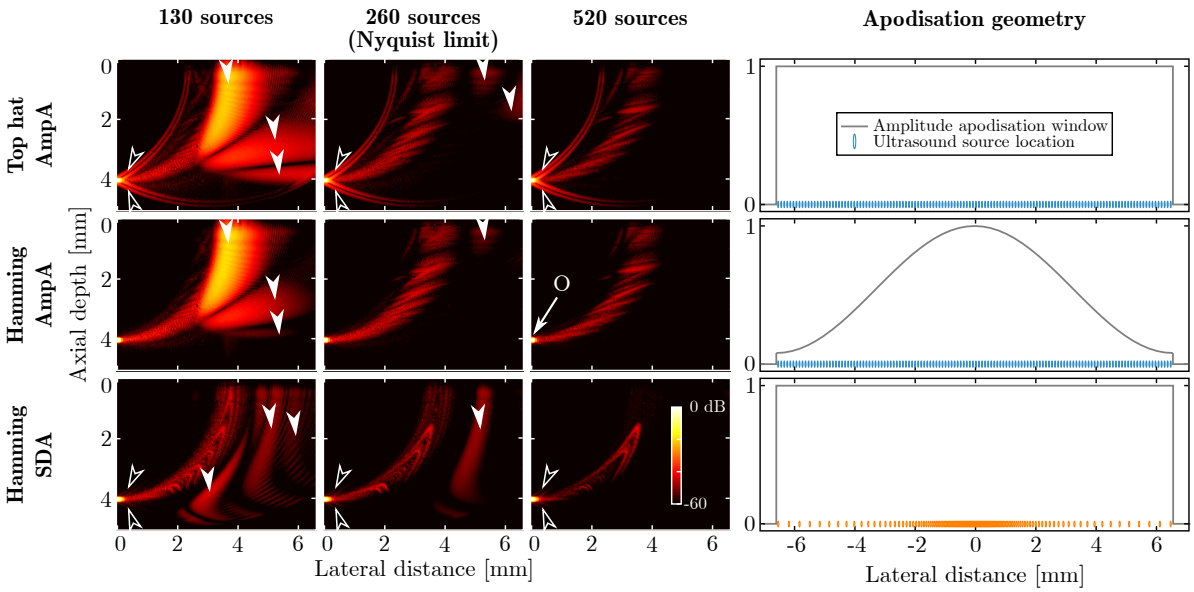

Fig. 4. **Comparison of amplitude apodisation and source density apodisation. Left nine panels:** Simulated all-optical ultrasound images of a single point scatterer using, from left to right, 130, 260 and 520 sources. In the top row these sources were distributed using top hat source density apodisation (SDA), resulting in periodic source spacing, and top hat amplitude apodisation (AmpA) was applied. In the middle row, top hat SDA was applied in conjunction with Hamming AmpA. In the bottom row, Hamming SDA was applied together with top hat AmpA. The images in the middle column (260 sources) were obtained using spatial sampling at the Nyquist limit (for a centre frequency of 15 MHz and an aperture of 13 mm). All six panels are shown using the same 60 dB dynamic range, normalised individually to each image. Solid arrow heads: grating lobes; open arrow heads: side lobes; O: object (present in all images, but indicated only once). The images are symmetric around the axial axis; for clarity only the positive lateral direction is shown. **Right graphs:** Schematics of the source positions (for arrays containing 130 sources) and amplitude apodisation windows W corresponding to the three rows of images.

lateral wire separation: 1 mm; axial layer separation: 3 mm) orthogonal to the image plane.

The same observations could be made when a tissue-mimicking phantom was used (Fig. 6). For these experiments, a solid phantom with a geometry based on the vasculature of a human placenta was fabricated in gelwax (comprising a mixture of mineral oil and glass microspheres to achieve physiological ultrasound speckle patterns) [25] and imaged using the same five apodisation functions. The highest resolution was observed for top hat SDA, followed by circular, triangular and Hamming SDA. For Hamming and triangular SDA, significant blurring in the lateral direction was observed. The image contrasts obtained using circular, Hamming and triangular SDA were similar, whilst that obtained using top hat SDA was significantly lower. Random SDA resulted in strong image artefacts that dominated the image, and hence rendered the phantom nearly invisible.

Spatial smoothness of the apodisation function

The poor imaging performance of random SDA observed in Figs. 5 and 6 can be understood from the properties of the corresponding spatial source density D: for randomised source positioning, D is likely to fluctuate strongly across the aperture (D is likely to be "spiky"; cf. Fig. 3). The power spectrum of D, which (as discussed in Section III) is predictive of the imaging performance of an apodisation scheme, is hence very broad as D contains a wide range of spatial frequencies, thereby giving rise to strong side lobes and corresponding image artefacts. Conversely, this implies that to achieve low side lobe levels, an apodisation function should mainly contain low spatial frequencies to ensure that the majority of the energy within its power spectrum is contained inside the main lobe. This requirement imposes limits on the tolerance of the source positioning, however, as significant deviation from the desired apodisation function introduces non-smoothness in the spatial source density. To illustrate this, simulated images of a point scatterer phantom were generated using circular SDA at various levels of source positioning inaccuracy (Fig. 7). For this experiment, B-scans were generated using laterally perturbed source coordinates, and images were reconstructed using the known and exact perturbed coordinates. As can be observed, image artefact levels increase with increasing source positioning perturbations. Further image artefacts can originate from the finite accuracy of the spatial calibration of the experimental setup and the associated uncertainty in the achieved source positions. Additional simulation studies (data not shown) revealed that imposing perturbations of the same magnitude as positioning *uncertainty* instead (i.e., B-scans were generated using the desired source locations, but images were reconstructed using perturbed source locations) yielded image artefacts of comparable shape and level, and in addition resulted in reduced image resolution. The discrepancy between images obtained from simulations and experiments observed in Fig. 5 can hence be attributed in part to spatial inaccuracy during source array synthesis, uncertainty in source locations during image reconstruction, and a difference in noise

0885-3010 (c) 2019 IEEE. Personal use is permitted, but republication/redistribution requires IEEE permission. See http://www.ieee.org/publications_standards/publications/rights/index.html for more information.

This article has been accepted for publication in a future issue of this journal, but has not been fully edited. Content may change prior to final publication. Citation information: DOI 10.1109/TUFFC.2019.2945636, IEEE Transactions on Ultrasonics, Ferroelectrics, and Frequency Control

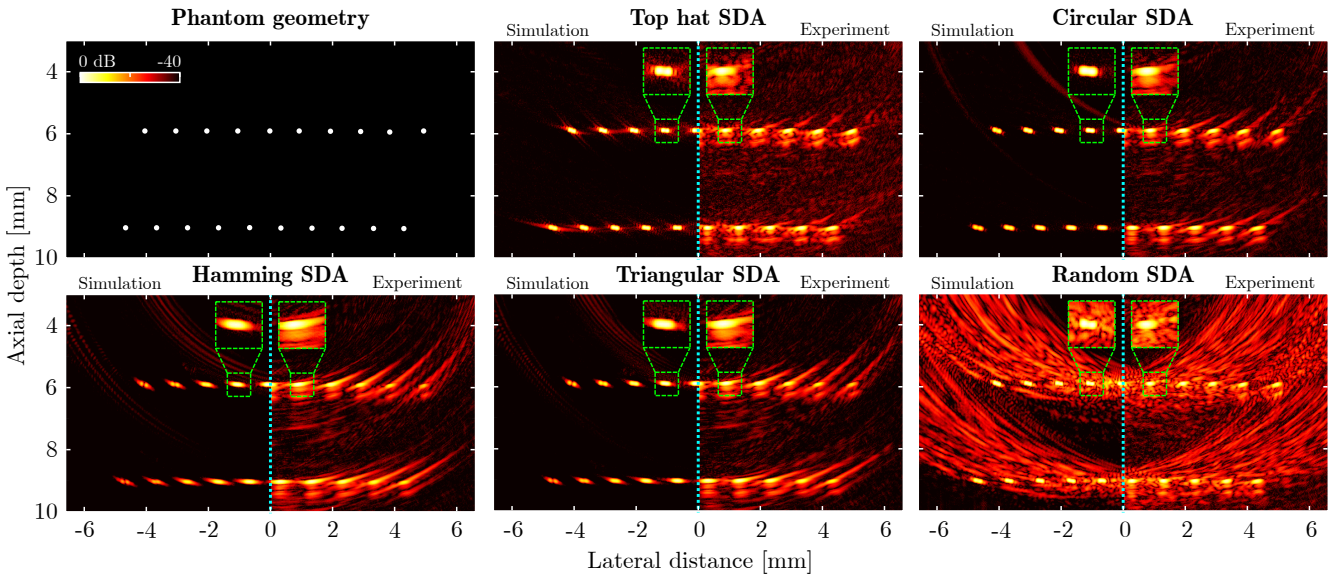

Fig. 5. **Resolution and image contrast for various source density apodisation (SDA) schemes. Top left:** Schematic of an imaging phantom comprising a number of point scatterers. **Remaining panels:** Simulated and experimentally obtained all-optical ultrasound images using, in clockwise orientation, top hat, circular, random, triangular and Hamming SDA. For each image, 260 sources were distributed across the source aperture. Each panel is displayed using a dynamic range of 40 dB, normalised separately to each image, and shows both simulated (left hand side of each panel) and experimentally obtained images (right hand side). Small regions were magnified (green inserts) to improve visibility. All images were reconstructed using top hat amplitude apodisation. The spatial source distribution for each SDA scheme is shown in Fig. 3.

characteristics.

Asymmetric apodisation

Most of the apodisation functions considered above were symmetric around the axial axis, and hence yielded symmetric imaging performance. However, to achieve low side lobe levels the apodisation function is only required to be smoothly varying; asymmetry might hence be used to control the image quality locally. As a final demonstration, a smoothly varying asymmetric SDA scheme is compared with a symmetric scheme to assess its usefulness for all-optical ultrasound imaging.

As symmetric SDA scheme, circular SDA is chosen for which the normalised lateral source coordinates are given by the trigonometric asin function: $x_{s,i} = 2\text{asin}(\chi_i)/\pi$, with χ_i a uniformly sampled quantity ranging between ± 1. For the asymmetric SDA scheme, an asymmetric source distribution is considered that is based on a stretched and laterally offset circular SDA scheme. For this asymmetric scheme, the normalised lateral source coordinates are given by $x_{s,i} = 2\text{asin}(\psi_i)/\pi$, where $\psi_i = \chi_i + 0.8(\chi_i + 10/13)^3$ is normalised to range between ± 1, resulting in the spatial source density shown in Fig. 8a. The parameters of ψ_i were chosen such that the maximum spatial source density of the asymmetric scheme occurred at a lateral coordinate of -3.5 mm, which coincides with the centre of the left half of the phantom.

Using asymmetric SDA, the left half of the resulting image shown in Fig. 8 (lateral coordinate ≤ 0 mm) exhibits better contrast ($+8$ dB and $+5$ dB at the left protrusion (solid arrow head) and far-left edge (open arrow head) of the image, respectively) and better fill-in than that obtained using circular SDA, and limited view artefacts (such as signal drop-out at lateral coordinates ≤ -5 mm, and poor definition of the outer edges of the vessels) have been partially overcome. However, these improvements are spatially localised: in the right half of the image the contrast is reduced (by up to 4 dB at the far-right edge (denoted by the asterisk) of the image) due to stronger artefacts, and limited view artefacts are more severe resulting in less fill-in. Asymmetric SDA schemes require the same number of pulse-echo acquisitions and hence the same acquisition time, but can provide superior local image quality in regions that can be dynamically positioned or even tracked across the image.

V. Discussion and Conclusion

In this work, we demonstrated how source density apodisation (SDA) is a viable alternative for conventional amplitude apodisation (AmpA). Using an all-optical ultrasound imaging setup capable of dynamically synthesising source apertures of arbitrary geometry, we showed both numerically and experimentally how SDA (resulting in non-uniform source pitch) and AmpA (applied to an array comprising periodically spaced sources) are equivalent in terms of side lobe suppression and resolution for large numbers of sources. However, for low numbers of sources, SDA yields superior image quality as grating lobe artefacts are largely avoided. SDA could thus be used to achieve high image quality at higher frame rates and lower data rates. These observations were shown in simulations (not reported here) to remain

0885-3010 (c) 2019 IEEE. Personal use is permitted, but republication/redistribution requires IEEE permission. See http://www.ieee.org/publications_standards/publications/rights/index.html for more information.

This article has been accepted for publication in a future issue of this journal, but has not been fully edited. Content may change prior to final publication. Citation information: DOI 10.1109/TUFFC.2019.2945636, IEEE Transactions on Ultrasonics, Ferroelectrics, and Frequency Control

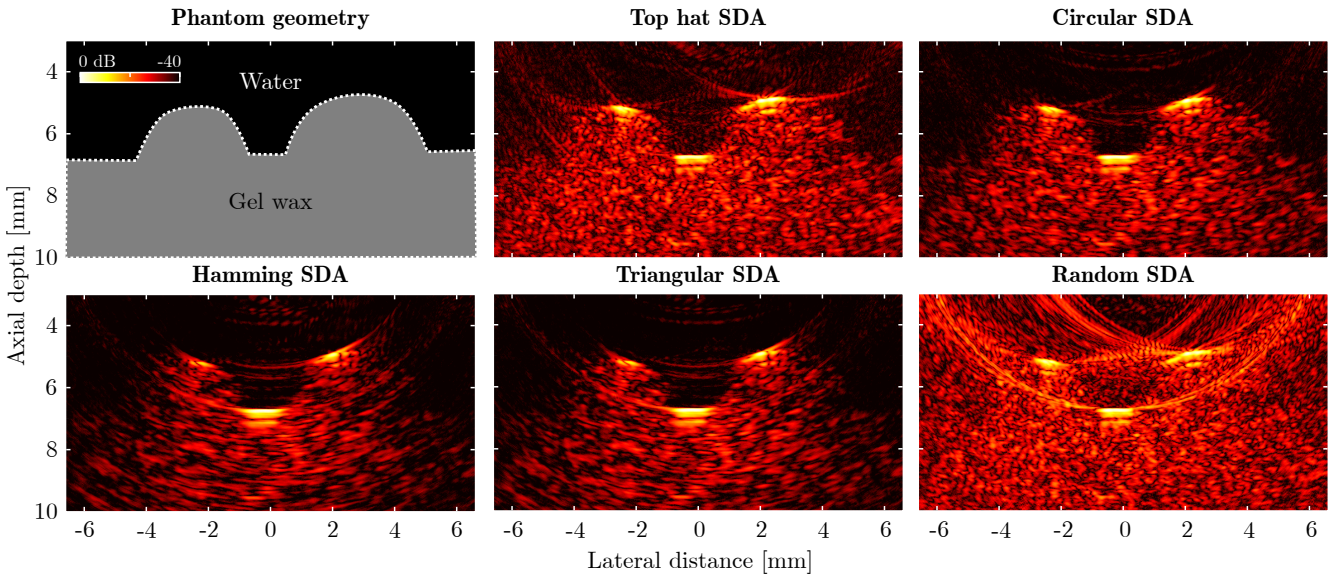

Fig. 6. **Performance of source density apodisation (SDA) for a tissue-mimicking phantom. Top left:** Schematic of a tissue-mimicking phantom modelled after human placental vasculature. **Remaining panels:** Experimentally obtained all-optical ultrasound images using, in clockwise orientation, top hat, circular, random, triangular and Hamming SDA. For each image, 260 sources were distributed across the source aperture. Each image was reconstructed using top hat amplitude apodisation and is displayed using an individually normalised dynamic range of 40 dB. The spatial source distribution for each SDA scheme is shown in Fig. 3.

valid for highly directional sources generating only ultrasound with frequencies $\geq$ 20 MHz. In addition, we demonstrated how asymmetric SDA patterns can be used to locally and dynamically optimise image quality. Furthermore, SDA and AmpA could be combined to obtain hybrid apodisation schemes that could further reduce the image artefacts.

The all-optical ultrasound imaging system used in this work allowed for arbitrary and non-periodic positioning of ultrasound sources with a lateral extent of 224 µm, which achieved weak source directivity and hence improved penetration depth. However, even the most sparsely populated arrays considered in this work resulted in an average source pitch of 100 µm. For all source arrays considered, consecutive source locations thus exhibited significant spatial overlap, which can reduce grating lobes [26, 27]. Spatially overlapping transducers can be achieved using conventional electronic transducers (for example using intricate electrode patterning with kerfless arrays, synthetic aperture scanning with a single transducer, or interleaved transducer elements [26]). However, the all-optical ultrasound imaging setup used here is, to the authors' knowledge, the only system capable of both video-rate 2D imaging and dynamic and arbitrary reconfiguration of the source array geometry, including asymmetric array geometries and spatially overlapping sources.

The best image quality was in this work obtained when spatially smoothly varying apodisation windows were used. Deviating from such smooth source densities, either deliberately through source position randomisation (to avoid grating lobes) or unintentionally due to positioning uncertainty or inaccuracy, was shown to lead to strong image artefacts. This observation is expected to extend to higher dimensional applications such as 3D imaging or high-intensity focussed ultrasound (HIFU), where sparsely populated 2D arrays are increasingly investigated to reduce probe complexity and data transfer rates [28, 29]. A commonly used method of achieving sparsity is to simply disregard or disconnect particular transducer elements within a periodically spaced array; however, this approach is equivalent to applying a spatially non-smooth binary AmpA function, which might result in strong side lobes and associated artefacts. In general, it can be expected that optimal image quality will be achieved with non-equidistantly spaced sparse arrays that incorporate SDA based on smoothly varying source density functions.

The SDA paradigm presented here could be beneficial for imaging probes comprising piezoelectric, capacitive and all-optical transducers alike, including ultra-fast imaging systems utilising plane wave excitation. However, it is especially well-suited for all-optical ultrasound imaging, where typically low numbers of optical receivers are used (in this work, a single receiver) and image artefacts could hence be more significant. In addition, an absence of distal electronics in all-optical ultrasound imaging probes greatly facilitates the synthesis of arbitrarily shaped imaging apertures, including those comprising spatially overlapping sources. The ability to dynamically and asymmetrically vary the source aperture geometry will enable dynamic, localised image optimisation to improve the visualisation of spatially dynamic procedures such as needle tracking. In addition, the dynamic reconfigurability of the source aperture will allow for the application of SDA to imaging probes based on linear arrays as well as to the phased arrays considered in this work. Through the use of a non-uniform source pitch, grating and side lobes can

0885-3010 (c) 2019 IEEE. Personal use is permitted, but republication/redistribution requires IEEE permission. See http://www.ieee.org/publications_standards/publications/rights/index.html for more information.

This article has been accepted for publication in a future issue of this journal, but has not been fully edited. Content may change prior to final publication. Citation information: DOI 10.1109/TUFFC.2019.2945636, IEEE Transactions on Ultrasonics, Ferroelectrics, and Frequency Control

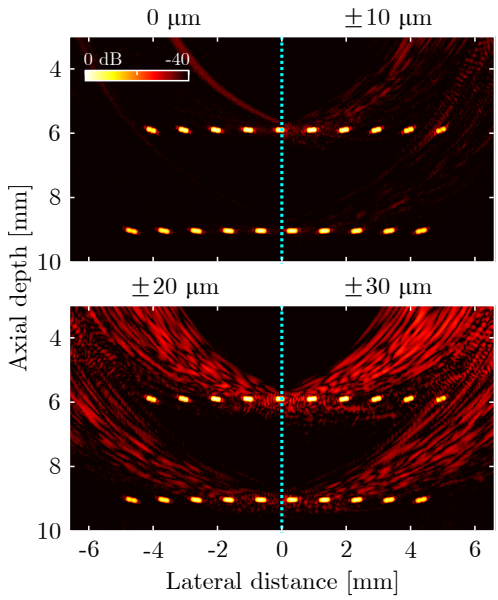

Fig. 7. **The impact of small perturbations in the source positioning.** Simulated all-optical ultrasound images of the phantom displayed in Fig. 5, obtained using 260 sources and circular source density apodisation (SDA). For these four images, the lateral coordinate of each source was slightly perturbed by adding a randomised offset generated from a uniform distribution. The range of this uniform distribution was set to, in clockwise orientation, 0 (corresponding to no perturbation), ±10, ±30 and ±20 µm. Each image is shown at an individually normalised dynamic range of 40 dB.

be simultaneously suppressed even for low channel counts, thus enabling high-quality imaging at high frame rates using acquisition systems of reduced complexity. SDA will be especially valuable in contexts where the use of densely sampled and fully populated transducer arrays is not feasible due to size or cost constraints.

References

[1] J. Jung, W. Lee, W. Kang, E. Shin, J. Ryu, and H. Choi, "Review of piezoelectric micromachined ultrasonic transducers and their applications," *Journal of Micromechanics and Microengineering*, vol. 27, no. 11, p. 113001, 2017.

[2] T. L. Szabo, *Diagnostic ultrasound imaging: inside out*. Elsevier Academic Press, 2004.

[3] R. J. Colchester, C. A. Mosse, D. S. Bhachu, J. C. Bear, C. J. Carmalt, I. P. Parkin, B. E. Treeby, I. Papakonstantinou, and A. E. Desjardins, "Laser-generated ultrasound with optical fibres using functionalised carbon nanotube composite coatings," *Applied Physics Letters*, vol. 104, no. 17, p. 173502, 2014.

[4] S.-L. Chen, "Review of laser-generated ultrasound transmitters and their applications to all-optical ultrasound transducers and imaging," *Applied Sciences*, vol. 7, no. 1, p. 25, 2016.

[5] S. Noimark, R. J. Colchester, B. J. Blackburn, E. Z. Zhang, E. J. Alles, S. Ourselin, P. C. Beard, I. Papakonstantinou, I. P. Parkin, and A. E. Desjardins, "Carbon-nanotube-PDMS composite coatings on optical fibres for all-optical ultrasound imaging," *Advanced Functional Materials*, vol. 26, no. 35, 2016.

[6] R. K. Poduval, S. Noimark, R. J. Colchester, T. J. Macdonald, I. P. Parkin, A. E. Desjardins, and I. Papakonstantinou, "Optical fiber ultrasound transmitter with electrospun carbon nanotube-polymer composite," *Applied Physics Letters*, vol. 110, no. 22, p. 223701, 2017.

[7] S. Noimark, R. J. Colchester, R. K. Poduval, E. Maneas, E. J. Alles, T. Zhao, E. Z. Zhang, M. Ashworth, E. Tsolaki, and A. H. Chester, "Polydimethylsiloxane composites for optical ultrasound generation and multimodality imaging," *Advanced Functional Materials*, vol. 28, no. 9, 2018.

[8] R. J. Colchester, E. J. Alles, and A. E. Desjardins, "A directional fibre optic ultrasound transmitter based on a reduced graphene oxide and polydimethylsiloxane composite," *Applied Physics Letters*, vol. 114, no. 11, p. 113505, 2019.

[9] Y. Hou, J.-S. Kim, S.-W. Huang, S. Ashkenazi, L. Jay Guo, and M. O'Donnell, "Characterization of a broadband all-optical ultrasound transducer-from optical and acoustical properties to imaging," *Ultrasonics, Ferroelectrics, and Frequency Control, IEEE Transactions on*, vol. 55, no. 8, pp. 1867–1877, 2008.

[10] E. Biagi, S. Cerbai, L. Masotti, L. Belsito, A. Roncaglia, G. Masetti, and N. Speciale, "Fiber optic broadband ultrasonic probe for virtual biopsy: Technological solutions," *Journal of Sensors*, vol. 2010, 2010.

[11] B.-Y. Hsieh, S.-L. Chen, T. Ling, L. J. Guo, and P.-C. Li, "All-optical scanhead for ultrasound and photoacoustic imaging - imaging mode switching by dichroic filtering," *Photoacoustics*, vol. 2, no. 1, pp. 39–46, 2014.

[12] C. Sheaff and S. Ashkenazi, "Polyimide-etalon all-optical ultrasound transducer for high frequency applications," in *Proceedings SPIE BiOS*, pp. 89434M–89434M–8, International Society for Optics and Photonics, 2014.

[13] S. M. Leinders, W. J. Westerveld, J. Pozo, P. L. M. J. van Neer, B. Snyder, P. O'Brien, H. P. Urbach, N. de Jong, and M. D. Verweij, "A sensitive optical micro-machined ultrasound sensor (OMUS) based on a silicon photonic ring resonator on an acoustical membrane," *Scientific Reports*, vol. 5, 2015.

[14] J. A. Guggenheim, J. Li, T. J. Allen, R. J. Colchester, S. Noimark, O. O. Ogunlade, I. P. Parkin, I. Papakonstantinou, A. E. Desjardins, E. Z. Zhang, and P. C. Beard, "Ultrasensitive plano-concave optical microresonators for ultrasound sensing," *Nature Photonics*, vol. 11, no. 11, pp. 714–719, 2017.

[15] E. J. Alles, S. Noimark, E. Maneas, E. Z. Zhang, I. P. Parkin, P. C. Beard, and A. E. Desjardins, "Video-rate all-optical ultrasound imaging," *Biomedical Optics Express*, vol. 9, no. 8, pp. 3481–3494, 2018.

[16] E. J. Alles, S. Noimark, E. Maneas, W. Xia, E. Z. Zhang, P. C. Beard, I. P. Parkin, and A. E. Desjardins, "Source

0885-3010 (c) 2019 IEEE. Personal use is permitted, but republication/redistribution requires IEEE permission. See http://www.ieee.org/publications_standards/publications/rights/index.html for more information.

This article has been accepted for publication in a future issue of this journal, but has not been fully edited. Content may change prior to final publication. Citation information: DOI 10.1109/TUFFC.2019.2945636, IEEE Transactions on Ultrasonics, Ferroelectrics, and Frequency Control

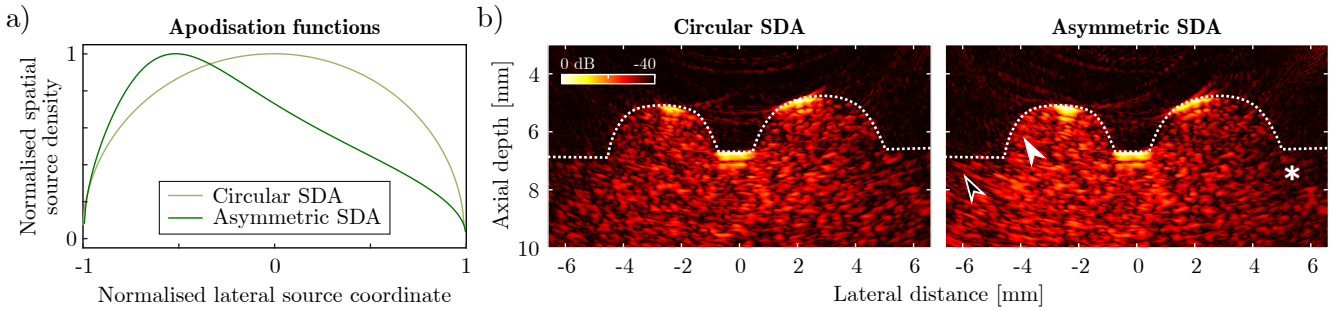

Fig. 8. **Asymmetric source density apodisation (SDA) enables local image quality optimisation. a)** Normalised spatial source densities for circular (light green) and asymmetric SDA (dark green). These apodisation functions were used to distribute 260 sources across the aperture. **b)** All-optical ultrasound images of a gelwax phantom obtained using circular (left) and asymmetric SDA (right). Each image is shown at an individually normalised dynamic range of 40 dB. Open and solid arrow heads: regions of improved contrast; ∗: region of reduced contrast. Dashed lines: boundary of the phantom.

density apodisation in 2D all-optical ultrasound imaging," in *Proceedings IEEE IUS*, pp. 1–4, IEEE, 2017.

[17] P. C. Beard, "Biomedical photoacoustic imaging," *Interface Focus*, vol. 1, no. 4, pp. 602–631, 2011.

[18] E. Z. Zhang and P. C. Beard, "Characteristics of optimized fibre-optic ultrasound receivers for minimally invasive photoacoustic detection," in *Proceedings SPIE BiOS*, pp. 932311–932311–9, International Society for Optics and Photonics, 2015.

[19] R. J. McGough, "Rapid calculations of time-harmonic nearfield pressures produced by rectangular pistons," *The Journal of the Acoustical Society of America*, vol. 115, no. 5, pp. 1934–1941, 2004.

[20] R. J. McGough, "FOCUS: Fast Object-Oriented C++ Ultrasound Simulator, www.egr.msu.edu/~fultras-web/index.php." Accessed: 24 May 2019.

[21] M. Karaman, P.-C. Li, and M. O'Donnell, "Synthetic aperture imaging for small scale systems," *Ultrasonics, Ferroelectrics, and Frequency Control, IEEE Transactions on*, vol. 42, no. 3, pp. 429–442, 1995.

[22] J. A. Jensen, S. I. Nikolov, K. L. Gammelmark, and M. H. Pedersen, "Synthetic aperture ultrasound imaging," *Ultrasonics*, vol. 44, pp. e5–e15, 2006.

[23] N. Bilaniuk and G. Wong, "Speed of sound in pure water as a function of temperature," *The Journal of the Acoustical Society of America*, vol. 93, no. 3, pp. 1609–1612, 1993.

[24] K. J. Parker, "Correspondence: apodization and windowing functions," *Ultrasonics, Ferroelectrics, and Frequency Control, IEEE Transactions on*, vol. 60, no. 6, pp. 1263–1271, 2013.

[25] E. Maneas, W. Xia, D. I. Nikitichev, B. Daher, M. Manimaran, R. Y. J. Wong, C.-W. Chang, B. Rahmani, C. Capelli, S. Schievano, G. Burriesci, S. Ourselin, A. L. David, M. C. Finlay, S. J. West, T. Vercauteren, and A. E. Desjardins, "Anatomically realistic ultrasound phantoms using gel wax with 3D printed moulds," *Physics in Medicine & Biology*, vol. 63, no. 1, 2018.

[26] F. J. Pompei and S.-C. Wooh, "Phased array element shapes for suppressing grating lobes," *The Journal of the Acoustical Society of America*, vol. 111, no. 5, pp. 2040–2048, 2002.

[27] V. Bavaro, G. Caliano, and M. Pappalardo, "Element shape design of 2-D CMUT arrays for reducing grating lobes," *Ultrasonics, Ferroelectrics, and Frequency Control, IEEE Transactions on*, vol. 55, no. 2, pp. 308–318, 2008.

[28] A. Ramalli, E. Boni, A. S. Savoia, and P. Tortoli, "Density-tapered spiral arrays for ultrasound 3-d imaging," *Ultrasonics, Ferroelectrics, and Frequency Control, IEEE Transactions on*, vol. 62, no. 8, pp. 1580–1588, 2015.

[29] E. Roux, F. Varray, L. Petrusca, C. Cachard, P. Tortoli, and H. Liebgott, "Experimental 3-d ultrasound imaging with 2-d sparse arrays using focused and diverging waves," *Scientific reports*, vol. 8, no. 1, p. 9108, 2018.

0885-3010 (c) 2019 IEEE. Personal use is permitted, but republication/redistribution requires IEEE permission. See http://www.ieee.org/publications_standards/publications/rights/index.html for more information.